

# Studies of granularity of a hadronic calorimeter for tens-of-TeV jets at a 100 TeV $pp$ collider

S.V. Chekanov<sup>a</sup>, A.V. Kotwal<sup>b,c</sup>, J. Proudfoot<sup>a</sup>, S. Sen<sup>b</sup>, N.V. Tran<sup>c</sup>, S.-S. Yu<sup>e</sup>,  
Chih-Hsiang Yeh<sup>e</sup>

<sup>a</sup> *HEP Division, Argonne National Laboratory, 9700 S. Cass Avenue, Argonne, IL 60439, USA.*

<sup>b</sup> *Department of Physics, Duke University, USA*

<sup>c</sup> *Fermi National Accelerator Laboratory*

<sup>d</sup> *Department of Physics, Michigan State University, 220 Trowbridge Road, East Lansing, MI 48824*

<sup>e</sup> *Department of Physics, National Central University, Chung-Li, Taoyuan City 32001, Taiwan*

---

## Abstract

Texts

*Keywords:* multi-TeV physics,  $pp$  collider, future hadron colliders, FCC, SppC

---

## 1. Introduction

Particle collisions at energies beyond those attained at the LHC will lead to many challenges for detector technologies. Future experiments, such as high-energy LHC (HE-LHC), future circular  $pp$  colliders of the European initiative, FCC-hh [1] and the Chinese initiative, SppC [2] will be required to measure high-momentum bosons ( $W$ ,  $Z$ ,  $H$ ) and top quarks with strongly collimated decay products that form jets. Studies of jet substructure can help identify such particles.

The reconstruction of jet substructure variables for collimated jets with transverse momentum above 10 TeV require an appropriate detector design. The most important for reconstruction of such jets are tracking and calorimeter. Recently, a number of studies [3, 4, 5] have been discussed using various fast simulation tools, such as Delphes [6], in which momenta of particles are smeared to mimic detector response.

A major step towards the usage of full Geant4 simulation to verify the granularity requirements for calorimeters was made in [7]. The studies included in this paper have illustrated a significant impact of granularity of electromagnetic (ECAL) and hadronic (HCAL) calorimeters on the shape of hadronic showers calculated using calorimeter hits for two particles separated by some angle. It was concluded that high granularity is essential in resolving two close-by particles for energies above 100 GeV.

This paper makes another step in understanding understanding of this problem in terms of high-level physics quantities typically used in physics analyses. Similar to the studies presented in [7], this paper is based on full Geant4 simulation with realistic jet reconstruction.

---

*Email addresses:* chekanov@anl.gov (S.V. Chekanov), ashutosh.kotwal@duke.edu (A.V. Kotwal), proudfoot@anl.gov (J. Proudfoot), sourav.sen@duke.edu (S. Sen), ntran@fnal.gov (N.V. Tran), syu@cern.ch (S.-S. Yu), jwzuzelski18@gmail.com (Chih-Hsiang Yeh)

*Preprints:* XXX-XXX

*September 14, 2018*

## 2. Simulation of detector response and event reconstruction

The description of the detector and software used for this paper is discussed in [7]. We use the SiFCC detector geometry with a software package that represents a versatile environment for simulations of detector performance, testing new technology options, event reconstruction techniques for future 100 TeV colliders.

The GEANT4 (version 10.3) [8] simulation of calorimeter response was complemented with the full reconstruction of calorimeter clusters formed by the Pandora algorithm [9, 10]. Calorimeter clusters were built from calorimeter hits in the ECAL and HCAL after applying the corresponding sampling fractions. No other corrections are applied. Hadronic jets were reconstructed with the FASTJET package [11] using the anti- $k_T$  algorithm [12] with a distance parameter of 0.5.

In the following discussion, we use the simulations of a heavy  $Z'$  boson, a hypothetical gauge boson that arises from extensions of the electroweak symmetry of the Standard Model. The  $Z'$  bosons were simulated with the masses,  $M = 5, 10, 20$  and 40 TeV. The lowest value represents a typical mass that is within the reach of the LHC experiments. The value 40 TeV represents the physics reach of 100 TeV colliders. The  $Z'$  particles are forced to decay to two light-flavor jets ( $q\bar{q}$ ),  $W^+W^-$  or  $t\bar{t}$ , where  $W$  and  $t$  decay hadronically. In all such scenarios, two highly boosted jets are produced, which are typically back-to-back in the laboratory frame. Typical transverse momenta of such jets are  $\simeq M/2$ . The main difference between considered decay types lays in different jet substructure. In the case of the  $q\bar{q}$  decays, jets do not have any internal structure. In the case of  $W^+W^-$ , each jet originates from  $W$ , thus it has two subjects because of the decay  $W \rightarrow q\bar{q}$ . In the case of hadronic top decays, jets have three subjects due to the decay  $t \rightarrow W^+ b \rightarrow q\bar{q}b$ . The signal events were generated using the PYTHIA8generator with the default settings, ignoring interference with SM processes. The event samples used in this paper are available from the HepSim database [13].

## 3. Studies of jet properties

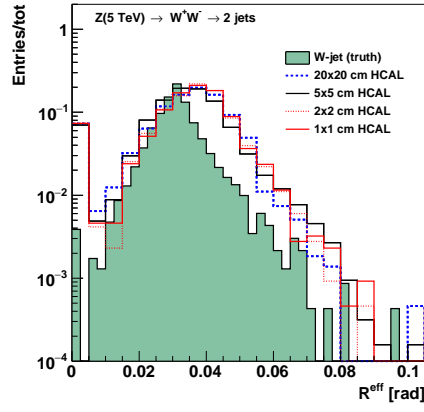
First let us consider several variables that represent jet substructure using different types of calorimeter granularity. The question we want to answer is how close the reconstructed jet substructure variables to the input "truth" value that are reconstructed using input particles directly from the PYTHIA8generator.

The effective radius is the average of the energy weighted radial distance in  $\eta - \phi$  space of jet constituents. Recently, it has been studied for multi-TeV jets in Ref.[14].

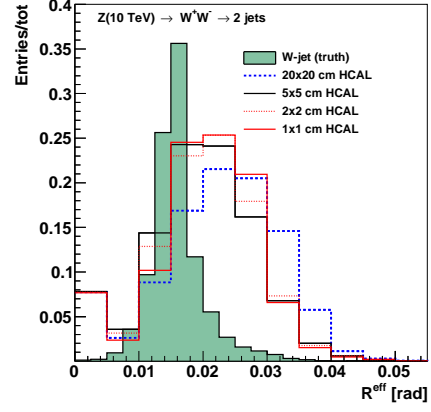
Let us study the effect of granularity on jet splitting scales. A jet  $k_T$  splitting scale [15] is defined as a distance measure used to form jets by the  $k_T$  recombination algorithm [16, 17]. This has been studied by ATLAS [18], and more recently in the context of 100 TeV physics [14]. The distribution of the splitting scale  $\sqrt{d_{12}} = \min(p_T^1, p_T^2) \times \delta R_{12}$  [18] at the final stage of the  $k_T$  clustering, where two subjects are merged into the final one, is shown in Fig. 2.

### 3.1. Jet subjetteness

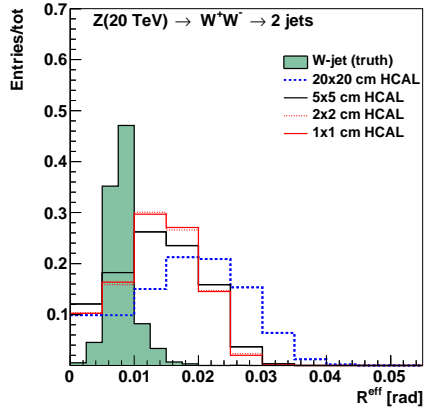
We recall that  $N$ -subjetteness [? 19],  $\tau_N$ , of jets has been proposed as a class of variables with which to study the decay products of a heavy particle inside jets.  $\tau_N$  is



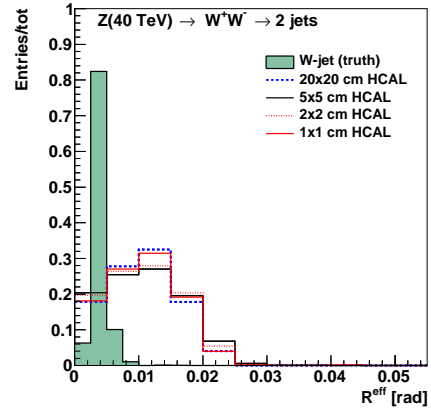
(a) 5 TeV



(b) 10 TeV

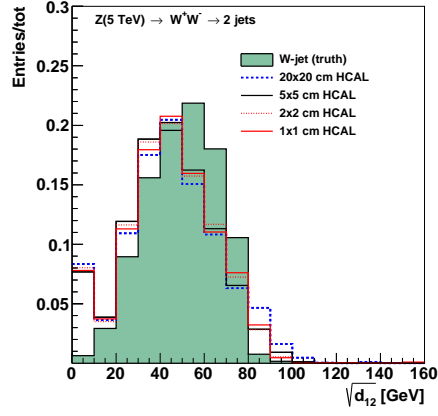


(c) 20 TeV

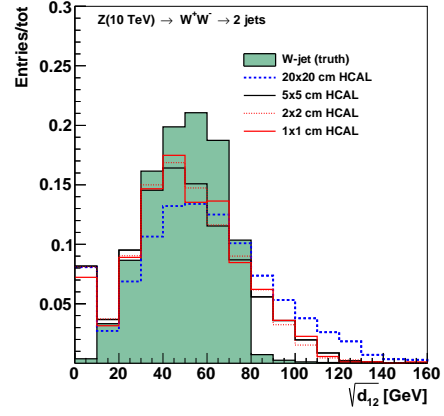


(d) 40 TeV

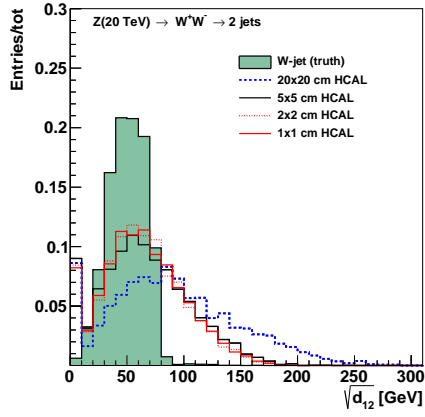
Figure 1: Jet effective radius for different jet transverse moment and HCAL granularity.



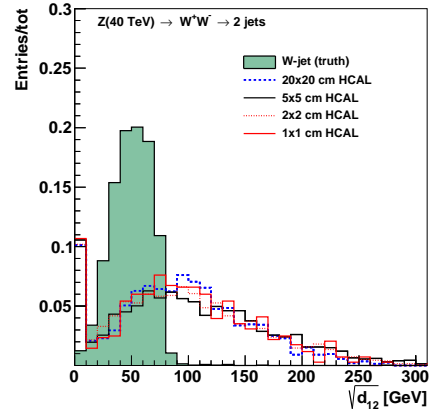
(a) 5 TeV



(b) 10 TeV



(c) 20 TeV



(d) 40 TeV

Figure 2: Jet splitting scale for different jet transverse moment and HCAL granularity.

a measure of the degree to which a jet can be considered as being composed of  $N$   $k_T$ -subjets [19]. The variable  $\tau_{32}$ , defined as the ratio of the  $N$ -subjettiness variables  $\tau_3/\tau_2$ , is particularly sensitive to hadronically-decaying top-quark initiated jets. The variable,  $\tau_{21} \equiv \tau_2/\tau_1$  can be used to reject background from  $W/Z$  decays. These variables do not strongly correlate with jet mass and can provide an independent check for the presence of top quarks. The jet substructure variables were obtained by re-running the  $k_T$  algorithm over the jet constituents of anti- $k_T$  jets.

#### 4. Study of detector performance with soft drop mass

In this section, we use the jet mass computed with a specific algorithm, soft drop declustering, to study the performance of detector with various detector cell sizes and center-of-mass (c.m.) energies.

##### 4.1. The technique of soft drop declustering

The soft drop declustering [20] is a grooming method that removes soft wide-angle radiation from a jet. The constituents of a jet  $j_0$  are first reclustered using the Cambridge-Aachen (C/A) algorithm [21, 22]. Then, the jet  $j_0$  is broken into two subjets  $j_1$  and  $j_2$  by undoing the last stage of C/A clustering. If the subjets pass the following soft drop condition, jet  $j_0$  is the final soft-drop jet. Otherwise, the algorithm redefines  $j_0$  to be the subjet with larger  $p_T$  (among  $j_1$  and  $j_2$ ) and iterates the procedure.

$$\frac{\min(p_{T1}, p_{T2})}{p_{T1} + p_{T2}} > z_{\text{cut}} \left( \frac{\Delta R_{12}}{R_0} \right)^\beta, \quad (1)$$

where  $p_{T1}$  and  $p_{T2}$  are the transverse momenta of the two subjets,  $z_{\text{cut}}$  is soft drop threshold,  $\Delta R_{12}$  is the distance between the two subjets in the  $\eta$ - $\phi$  plane,  $R_0$  is the characteristic radius of the original jet, and  $\beta$  is the angular exponent.

In our study, we compare the performance of future detector when setting  $\beta = 0$  versus when setting  $\beta = 2$ . For  $\beta = 0$ , the soft drop condition depends only on the  $z_{\text{cut}}$ . For  $\beta = 2$ , the condition depends on the angular distance between the two subjets and  $z_{\text{cut}}$  and the algorithm becomes infrared and collinear safe.

##### 4.2. Analysis method

We employ the following method to quantify the detector performance and find out the cell size that gives the best separation power to distinguish signal from background. For each configuration of detector and c.m. energy, we draw the receiver operating characteristic (ROC) curves in which the x-axis is the signal efficiency ( $\epsilon_{\text{sig}}$ ) and y-axis is the inverse of background efficiency ( $1/\epsilon_{\text{bkg}}$ ). In order to scan the efficiencies of soft drop mass cuts, we vary the mass window as follows. We first look for the median bin  $i_{\text{med}}$ <sup>1</sup> of the soft drop mass histogram from simulated signal events. Taking the right boundary of bin  $i_{\text{med}}$  as the center of mass window  $x_{\text{center}}$ , we start increasing the width of mass window symmetrically on the left and on the right of  $x_{\text{center}}$ , in steps of

<sup>1</sup>The integral from bin 0 to bin  $i_{\text{med}}$  ( $i_{\text{med}} - 1$ ) should be greater (less) than half of the total number of events. Note, the bin width is 5 GeV.

5 GeV, i.e. the narrowest mass window is  $[x_{\text{center}} - 5, x_{\text{center}} + 5]$ . If one side reaches the boundary of the mass histogram, we only increase the width on the other side, also in steps of 5 GeV. For each mass window, there will be corresponding  $\epsilon_{\text{sig}}$  and  $\epsilon_{\text{bkg}}$ , which gives a point in the ROC curves.

#### 4.3. Results and conclusion

Figures 3, 5, 7, and 9 present the distributions of soft drop mass for  $\beta = 0$  and  $\beta = 2$  with different c.m. energies and detector cell sizes; the signals considered are  $Z' \rightarrow WW$  and  $Z' \rightarrow t\bar{t}$ . In Figs. 4, 6, 8, and 10, ROC curves from different detector cell sizes are compared for each c.m. energy, respectively.

Figures 4 and 6 show that for  $\beta = 0$  the smallest detector cell size,  $1 \text{ cm} \times 1 \text{ cm}$ , has the best separation power at  $\sqrt{s} = 5, 10$ , and  $20 \text{ TeV}$  when the signal is  $Z' \rightarrow WW$  and at  $\sqrt{s} = 10$  and  $20 \text{ TeV}$  when the signal is  $Z' \rightarrow t\bar{t}$ . On the contrary, Figs. 8 and 10 show that for  $\beta = 2$  the smallest detector cell size does not have improvements in the separation power with respect to those with larger cell sizes. In fact, the performances of the three cell sizes are similar. In addition, sometimes bigger detector cell sizes,  $5 \text{ cm} \times 5 \text{ cm}$  or  $20 \text{ cm} \times 20 \text{ cm}$  have the best separation power.

We also find compared to  $\beta = 2$ , soft drop mass with  $\beta = 0$  has better performance for distinguishing signal from background. Therefore, we will apply requirements on this variable when studying the other jet substructure variables.

### 5. Studies of signal and background separation using jet substructure variables

In this section, we study different jet substructure variables and compare their ability to separate signal from background with different detector sizes and c.m. energy using Mann-Whitney U test and ROC curves.

By definition of Mann Whitney U test, if U value is close to 0.5, it means two distributions have similar compositions, and we can not distinguish them very well. On the other hand, if U value of two distributions are close to 0, it means both compositions of both distribution are much different from each other.

#### 5.1. N-subjettiness

N-subjettiness[??] is the detection technique of jet substructure that is used to identify boosted hadronically-decaying objects under the high c.m. conditions. We use  $\tau$  variable to distinguish the number of subjet in a fatjet to separate signal and background with different detector sizes and c.m. energy.

##### 5.1.1. The technic of N-subjettiness

The formula and the technique are as following:

$$\tau_N = \frac{1}{d_0} \sum_k p_{T,k} \min\{\Delta R_{1,k}, \Delta R_{2,k}, \dots, \Delta R_{N,k}\} \quad (2)$$

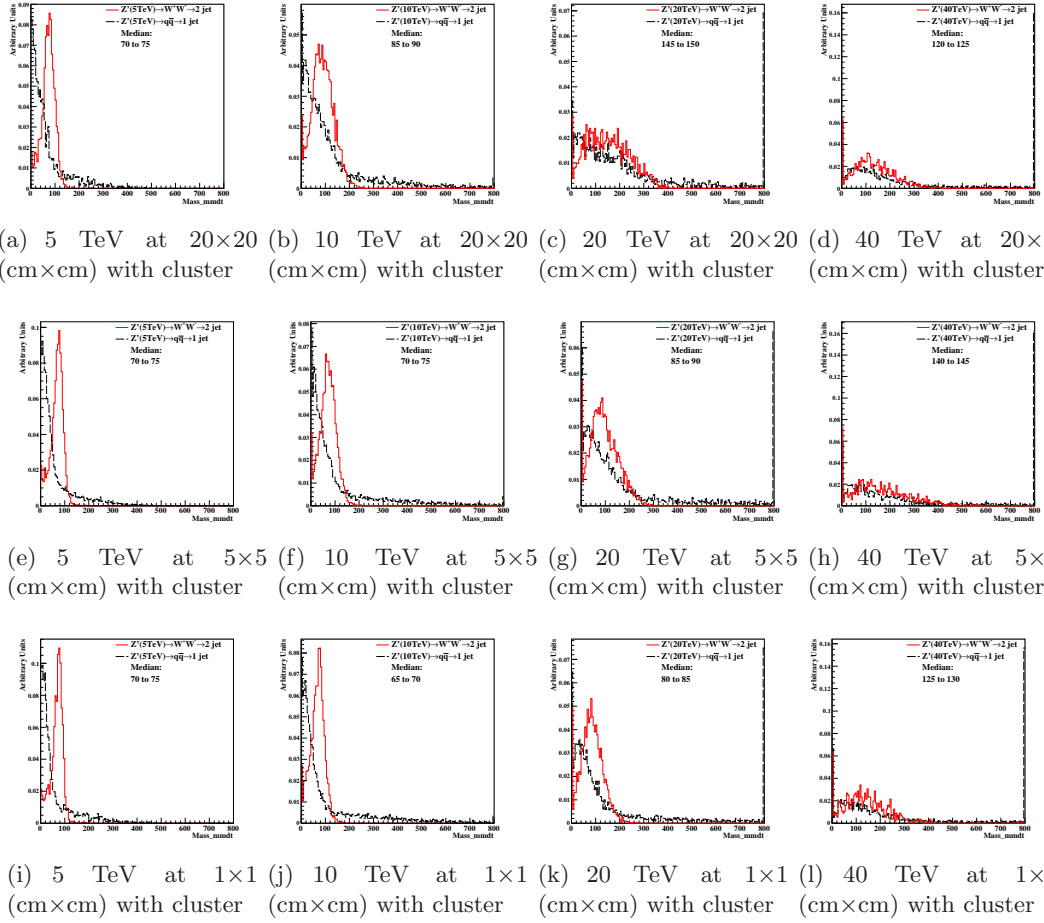
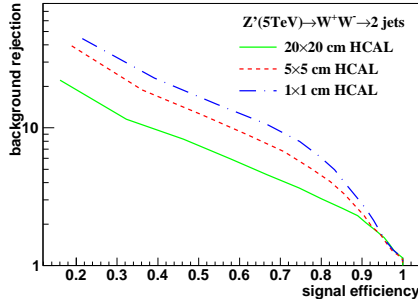
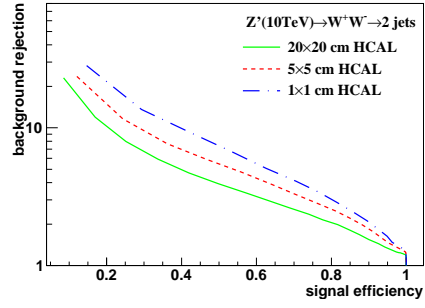


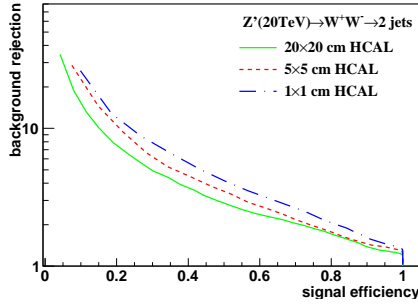
Figure 3: Distributions of soft drop mass for  $\beta=0$ , with 5, 10, 20, and 40 TeV c.m. energies and three different detector cell sizes:  $20 \times 20$ ,  $5 \times 5$ , and  $1 \times 1$  (cm $\times$ cm). The signal (background) process is  $Z' \rightarrow WW$  ( $Z' \rightarrow qq$ ).



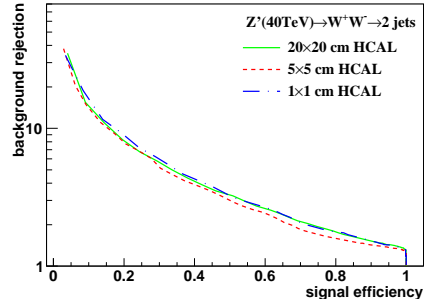
(a) Central at Median( $20 \times 20 = 5 \times 5 = 1 \times 1$ ) change width with cluster at 5 TeV



(b) Central at Median( $20 \times 20 = 5 \times 5 = 1 \times 1$ ) change width with cluster at 10 TeV



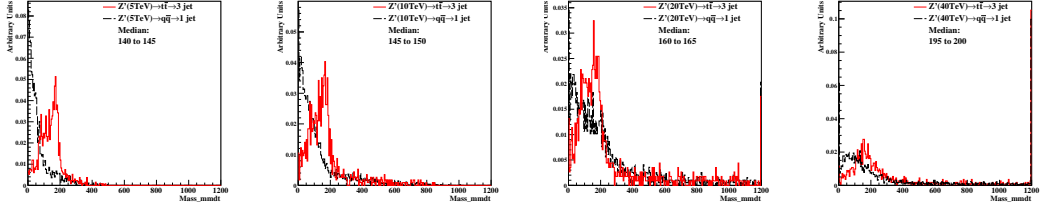
(c) Central at Median( $20 \times 20 = 5 \times 5 = 1 \times 1$ ) change width with cluster at 20 TeV



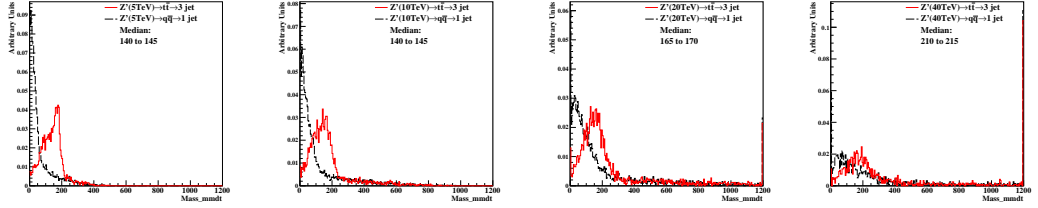
(d) Central at Median( $20 \times 20 = 5 \times 5 = 1 \times 1$ ) change width with cluster at 40 TeV

Figure 4: The ROC curves of soft drop mass selection for  $\beta=0$  with 5, 10, 20, and 40 TeV c.m. energies. Three different detector cell sizes are compared:  $20 \times 20$ ,  $5 \times 5$ , and  $1 \times 1$  (cm $\times$ cm). The signal (background) process is  $Z' \rightarrow WW$  ( $Z' \rightarrow q\bar{q}$ ).

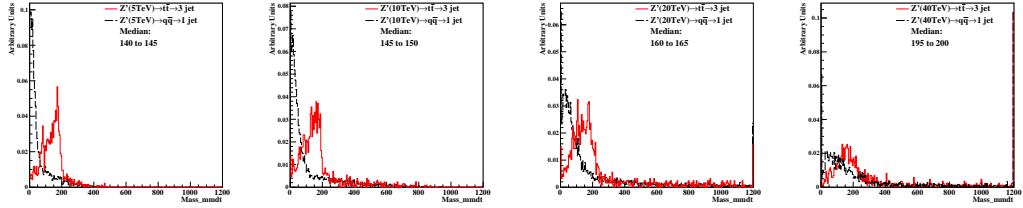




(a) 5 TeV at  $20 \times 20$  (b) 10 TeV at  $20 \times 20$  (c) 20 TeV at  $5 \times 5$  (d) 40 TeV at  $5 \times 5$   
(cm $\times$ cm) with cluster (cm $\times$ cm) with cluster (cm $\times$ cm) with cluster (cm $\times$ cm) with cluster

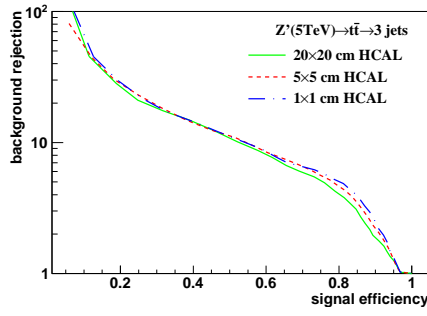


(e) 5 TeV at  $1 \times 1$  (f) 10 TeV at  $1 \times 1$  (g) 20 TeV at  $20 \times 20$  (h) 40 TeV at  $20 \times 20$   
(cm $\times$ cm) with cluster (cm $\times$ cm) with cluster (cm $\times$ cm) with cluster (cm $\times$ cm) with cluster

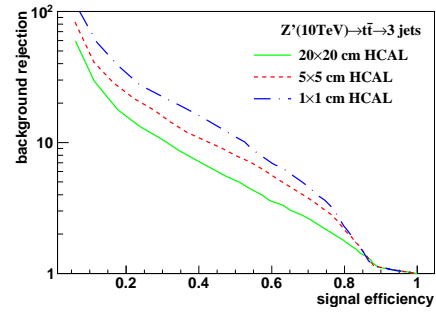


(i) 5 TeV at  $5 \times 5$  (j) 10 TeV at  $5 \times 5$  (k) 20 TeV at  $1 \times 1$  (l) 40 TeV at  $1 \times 1$   
(cm $\times$ cm) with cluster (cm $\times$ cm) with cluster (cm $\times$ cm) with cluster (cm $\times$ cm) with cluster

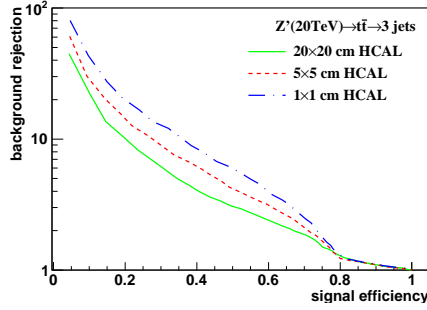
Figure 5: Distributions of soft drop mass for  $\beta=0$ , with 5, 10, 20, and 40 TeV c.m. energies and three different detector cell sizes:  $20 \times 20$ ,  $5 \times 5$ , and  $1 \times 1$  (cm $\times$ cm). The signal (background) process is  $Z' \rightarrow t\bar{t}$  ( $Z' \rightarrow q\bar{q}$ ).



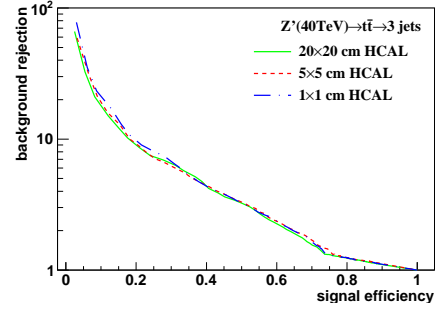
(a) Central at Median( $20 \times 20=, 5 \times 5=, 1 \times 1=$ ) change width with cluster at 5 TeV



(b) Central at Median( $20 \times 20=, 5 \times 5=, 1 \times 1=$ ) change width with cluster at 10 TeV



(c) Central at Median( $20 \times 20=, 5 \times 5=, 1 \times 1=$ ) change width with cluster at 20 TeV



(d) Central at Median( $20 \times 20=, 5 \times 5=, 1 \times 1=$ ) change width with cluster at 40 TeV

Figure 6: The ROC curves of soft drop mass selection for  $\beta=0$  with 5, 10, 20, and 40 TeV c.m. energies. Three different detector cell sizes are compared:  $20 \times 20$ ,  $5 \times 5$ , and  $1 \times 1$  (cm $\times$ cm). The signal (background) process is  $Z' \rightarrow t\bar{t}$  ( $Z' \rightarrow q\bar{q}$ ).

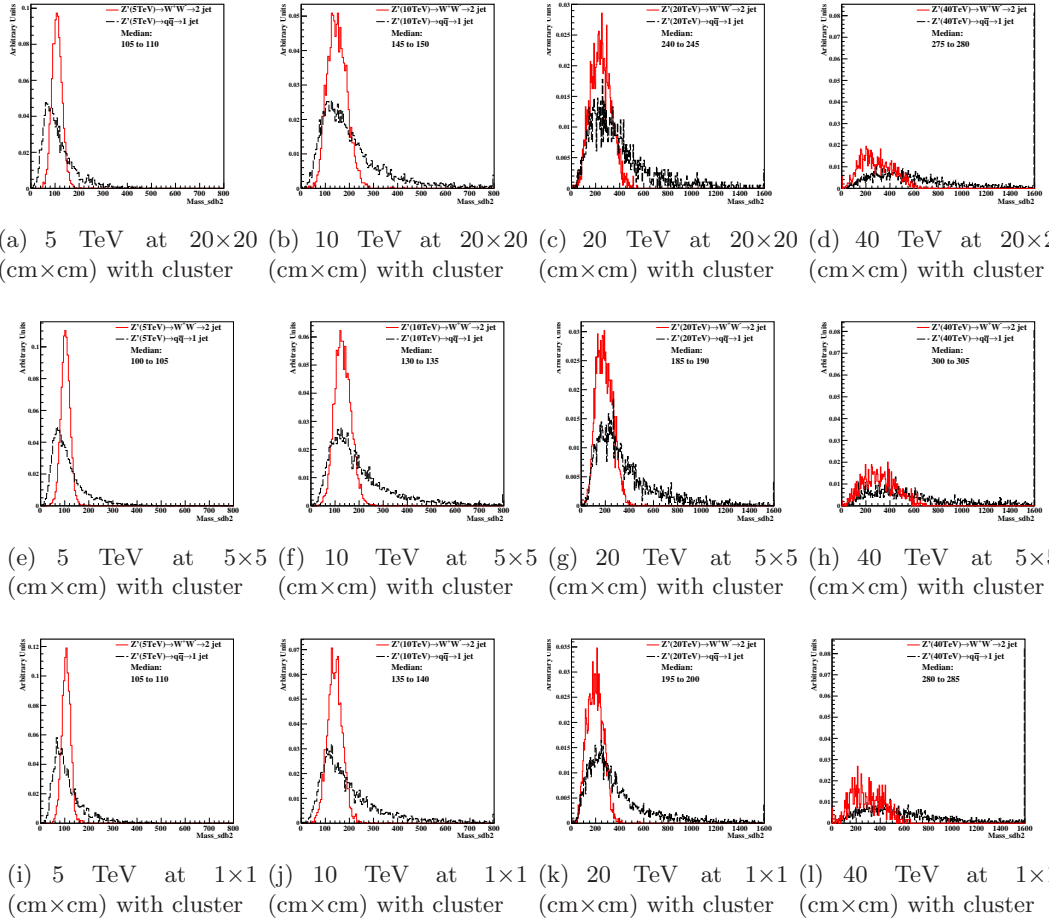
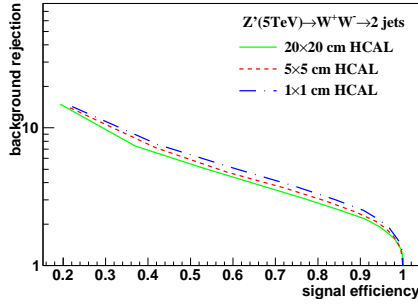
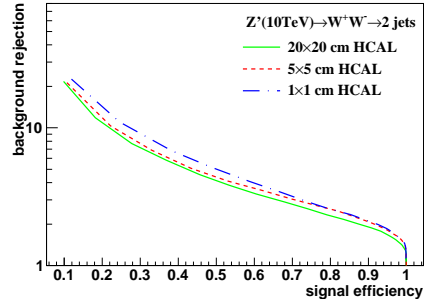


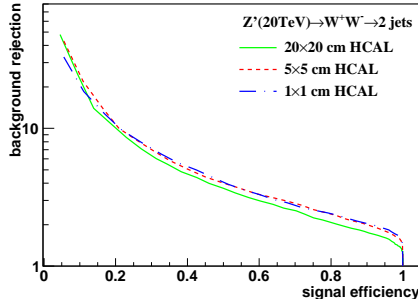
Figure 7: Distributions of soft drop mass for  $\beta=2$ , with 5, 10, 20, and 40 TeV c.m. energies and three different detector cell sizes: 20×20, 5×5, and 1×1 (cm×cm). The signal (background) process is  $Z' \rightarrow WW$  ( $Z' \rightarrow qq$ ).



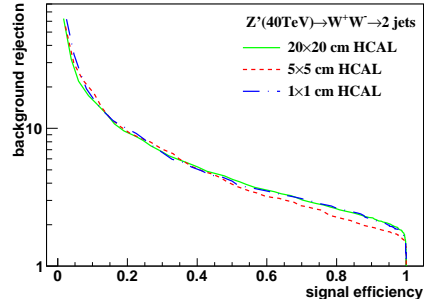
(a) Central at Median( $20 \times 20 = 5 \times 5 = 1 \times 1$ ) change width with cluster at 5 TeV



(b) Central at Median( $20 \times 20 = 5 \times 5 = 1 \times 1$ ) change width with cluster at 10 TeV



(c) Central at Median( $20 \times 20 = 5 \times 5 = 1 \times 1$ ) change width with cluster at 20 TeV



(d) Central at Median( $20 \times 20 = 5 \times 5 = 1 \times 1$ ) change width with cluster at 40 TeV

Figure 8: The ROC curves of soft drop mass selection for  $\beta=2$  with 5, 10, 20, and 40 TeV c.m. energies. Three different detector cell sizes are compared:  $20 \times 20$ ,  $5 \times 5$ , and  $1 \times 1$  (cm $\times$ cm). The signal (background) process is  $Z' \rightarrow WW$  ( $Z' \rightarrow q\bar{q}$ ).

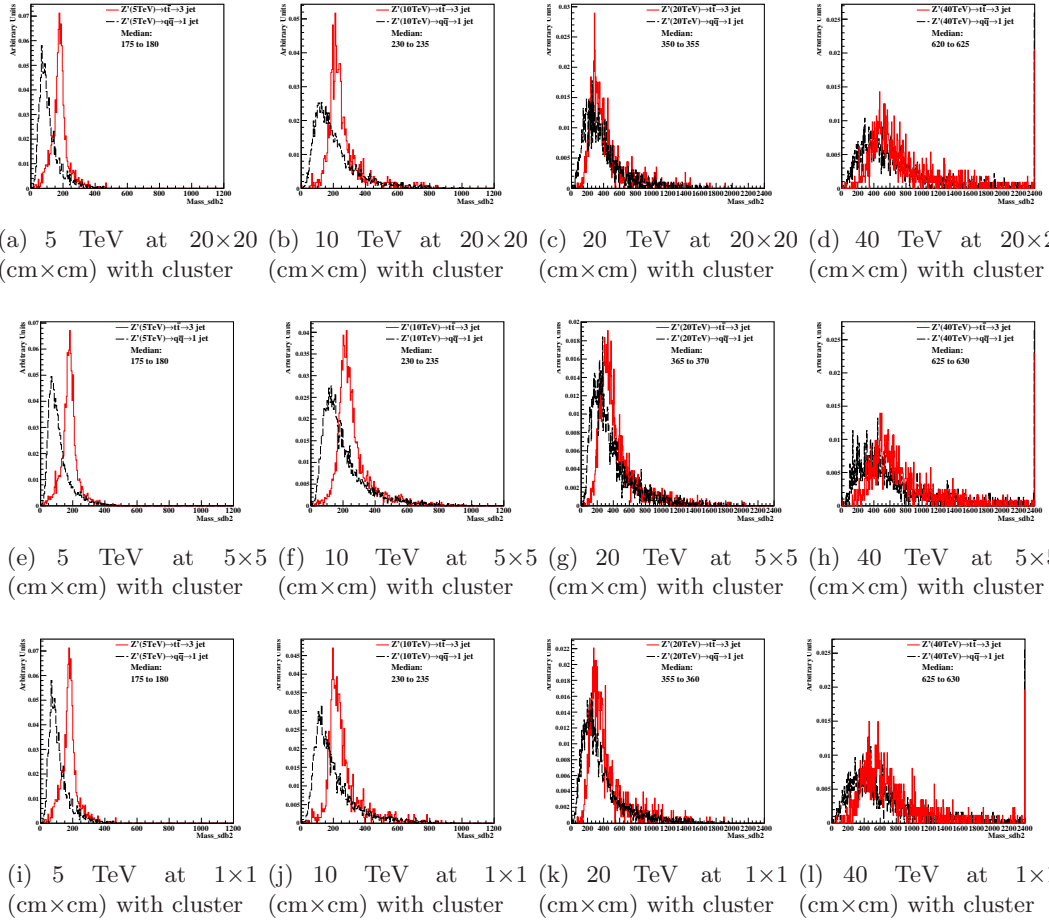
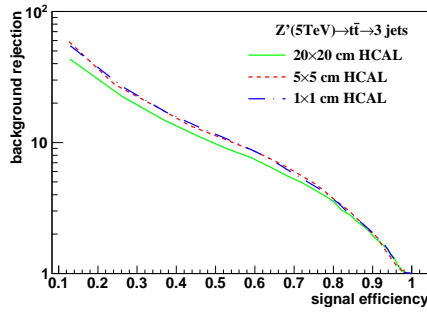
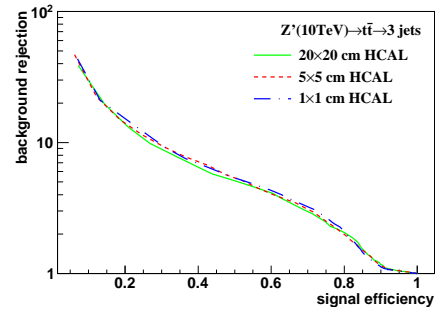


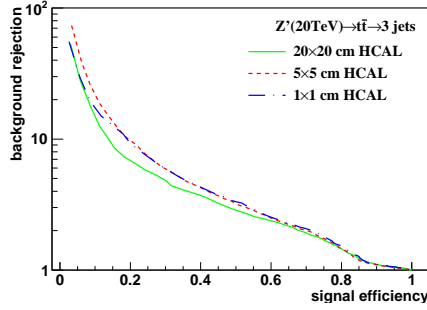
Figure 9: Distributions of soft drop mass for  $\beta=2$ , with 5, 10, 20, and 40 TeV c.m. energies and three different detector cell sizes: 20×20, 5×5, and 1×1 (cm×cm). The signal (background) process is  $Z' \rightarrow t\bar{t}$  ( $Z' \rightarrow q\bar{q}$ ).



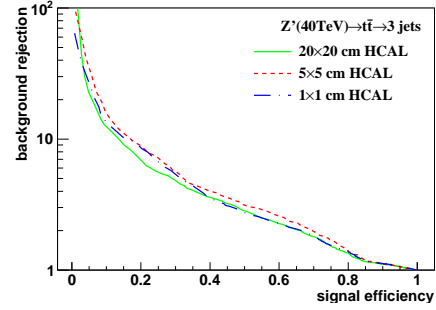
(a) Central at Median( $20 \times 20=, 5 \times 5=, 1 \times 1=$ ) change width with cluster at 5 TeV



(b) Central at Median( $20 \times 20=, 5 \times 5=, 1 \times 1=$ ) change width with cluster at 10 TeV



(c) Central at Median( $20 \times 20=, 5 \times 5=, 1 \times 1=$ ) change width with cluster at 20 TeV



(d) Central at Median( $20 \times 20=, 5 \times 5=, 1 \times 1=$ ) change width with cluster at 40 TeV

Figure 10: The ROC curves of soft drop mass selection for  $\beta=2$  with 5, 10, 20, and 40 TeV c.m. energies. Three different detector cell sizes are compared:  $20 \times 20$ ,  $5 \times 5$ , and  $1 \times 1$  (cm $\times$ cm). The signal (background) process is  $Z' \rightarrow t\bar{t}$  ( $Z' \rightarrow q\bar{q}$ ).

$$d_0 = \sum_k p_{T,k} R_0 \quad (3)$$

$k$  runs over all constituent particles in the given jets (fatjet),  $p_{T,k}$  are their transverse momentum,  $\Delta R_{J,k} = \sqrt{(\Delta\eta)^2 + (\Delta\phi)^2}$  is the distance between the constituent particles  $k$  and the candidate subjet  $J$  on the  $\eta - \phi$  plane.  $R_0$  is the characteristic jet radius used in Anti-kt(AK) jet algorithm at starting.  $d_0$  is the normalization factor.

1. First, Anti-kt(AK) algorithm is used to reconstruct jets
2. Second, after reconstructing the AK4 jets, exclusive  $k_T$  algorithm[??] is used in finding the jet axis in a fatjet.
3. Third, start running formula [2] and loop all constituent particles in a fatjet.
4. Finally, when finishing running all particles, it will give out  $\tau_N$ , where  $N$  is positive integer.

If a fatjet has  $N$  subjet(s)[??], its  $\tau_N$  is smaller than the  $\tau_N$  of the fatjet with different number of subjets. For example, if we compare the  $\tau_2$  of one-subjet fatjet and two-subjets one, two-subjets fatjet has smaller  $\tau_2$  than one-subjet one. On the other hand, one-subjet fatjet has smaller  $\tau_1$  than two-subjets one. In the end, we can use the ratio of  $\tau_2$  and  $\tau_1$  ( $\tau_{21}$ ) to distinguish fatjet with one-subjet case and two-subjets case.  $\tau_{21}$  is used to discriminate the fatjet shape, and it can be modified with different number of subjet.

In our study, we use  $\tau_{21}$  and  $\tau_{32}$  in distinguishing two-subjets fatjet and three-subjets fatjet from one-subjet fatjet individually. We want to use this two ratio values to distinguish signal from background.

### 5.1.2. Analysis method

First, we select the events in mass window by using SD with  $\beta = 0$  and 75% signal efficiency. Then, we find the highest ratio bin to be our seed bin. Next, we compare the left and right of ratio bin, and add the higher bin to be our width. Finally, We can use this width to draw the ROC curves.

2

### 5.1.3. The results and conclusion

In the figure [13][15], they show the histograms of  $\tau_{21}$  and  $\tau_{32}$  after selecting the events. In all figures, they also include the Mann-Whitney U value in ir the legend.

As a result of figure [14][16], they perform the ROC curves of  $\tau_{21}$  and  $\tau_{32}$  with different detector cell sizes and c.m. energy. The smallest detector cell ( $1 \times 1$ ) doesn't have the best separation power to distinguish signal from background. Some of them have the best separation power with the bigger cell size ( $5 \times 5$  and  $20 \times 20$ ).

In Figure [17](a)(b), they show the summary plots of  $\tau_{21}$  and  $\tau_{32}$  with the rawhit cut with 0.5GeV using Mann Whitney U test. In  $\tau_{21}$ , 5TeV has better separation power when detector sizes get smaller. When energy increases, there is no improvement in

the smallest detector cell size ( $1 \times 1$ ). In  $\tau_{32}$ , the case is similar to  $\tau_{21}$ . Even worse, with some c.m. energies, the bigger detector sizes ( $5 \times 5$  and  $20 \times 20$ ) have better separation power than the smallest detector sizes ( $1 \times 1$ ).

## 5.2. Studies of signal and background separation using jet substructure variable: Energy correlation function

Energy correlation function (ECF) [??] is another kind of detection technique of jet substructure that is used to distinguish the number of subjets in a fatjet under high c.m. energy conditions. This method only uses the momenta of particles and the angles between them without additional algorithm.

### 5.2.1. The technic of energy correlation function

The basic ECF formula is as following:

$$ECF(N, \beta) = \sum_{i_1 < i_2 < \dots < i_N \in J} \left( \prod_{a=1}^N E_{ia} \right) \left( \prod_{b=1}^{N-1} \prod_{c=b+1}^N \theta_{ibic} \right)^\beta \quad (4)$$

In the formula 4, the sum loop all particles in the jet  $J$ ,  $E$  are the energy of particles, and  $\theta$  are the angles between the particles.

We apply two approximation. First, because under the high energy limitation  $p \gg m$ ,  $E \approx p$ . Second, we use Radius  $R$  between particles naturally, so our ECF formula (4) can be modified to the formula:

$$ECF(N, \beta) = \sum_{i_1 < i_2 < \dots < i_N \in J} \left( \prod_{a=1}^N P_{ia} \right) \left( \prod_{b=1}^{N-1} \prod_{c=b+1}^N R_{ibic} \right)^\beta \quad (5)$$

From the modified ECF formula (5), in order to use the dimensionless observation to determine whether the number of subjets in system, parameter  $\tau_N$  is defined as:

$$\tau_N^{(\beta)} \equiv \frac{ECF(N+1, \beta)}{ECF(N, \beta)} \quad (6)$$

The idea of formula (6) is from N-subjetness, because the behavior of it is very similar to N-subjetness as reference [??]. In general, if the system has N subjets,  $ECF(N+1, \beta)$  should be significantly smaller than  $ECF(N, \beta)$ , so we can use this advantage to distinguish different number of subjets. Finally, because it is suggested to used  $\tau_{21}$ ,  $\tau_{32}$  [??] to distinguish two-subjets fatjet and three-subjets fatjet from one-subjet fatjet, in the ECF, it also defines the ratio of  $\tau$  there, and define the energy correlation double ratio that is used in our study:

$$C_N^{(\beta)} \equiv \frac{\tau_N^{(\beta)}}{\tau_{N-1}^{(\beta)}} = \frac{ECF(N-1, \beta) ECF(N+1, \beta)}{ECF(N, \beta)^2} \quad (7)$$

We set  $N=2$  and  $\beta = 1$  ( $C_2^1$ ) to distinguish two-subjets fatjet from one-subjet fatjet.



### 5.2.2. Analysis method

First, we select the events in mass window by using SD with  $\beta = 0$  and 75% signal efficiency. Then, we find the highest ratio bin to be our seed bin. Next, we compare the left and right of ratio bin, and add the higher bin to be our width. Finally, We can use this width to draw the ROC curves.

### 5.2.3. The results and conclusion

In the figure [11], they show the histograms of  $\tau_{21}$  and  $\tau_{32}$  after selecting the events. In all figures, they also include the Mann-Whitney U value in their legend

As a result of figure [12], they perform the ROC curves of  $C_2^1$  with different detector cell sizes and c.m. energy. The smallest detector cell ( $1 \times 1$ ) doesn't have the best separation power to distinguish signal from background. In addition, in some cases such like (a), the biggest one ( $20 \times 20$ ) has the best distinguish power under the same c.m. energy.

In Figure [17](c), it shows the summary plots with the rawhit cut with 0.5GeV using Mann Whitney U test. For conclusion, all separation power aren't improved by smallest cell size ( $1 \times 1$ ).

## Acknowledgements

This research was performed using resources provided by the Open Science Grid, which is supported by the National Science Foundation and the U.S. Department of Energy's Office of Science. We gratefully acknowledge the computing resources provided on Blues, a high-performance computing cluster operated by the Laboratory Computing Resource Center at Argonne National Laboratory. Argonne National Laboratory's work was supported by the U.S. Department of Energy, Office of Science under contract DE-AC02-06CH11357. The Fermi National Accelerator Laboratory (Fermilab) is operated by Fermi Research Alliance, LLC under Contract No. DE-AC02-07CH11359 with the United States Department of Energy.

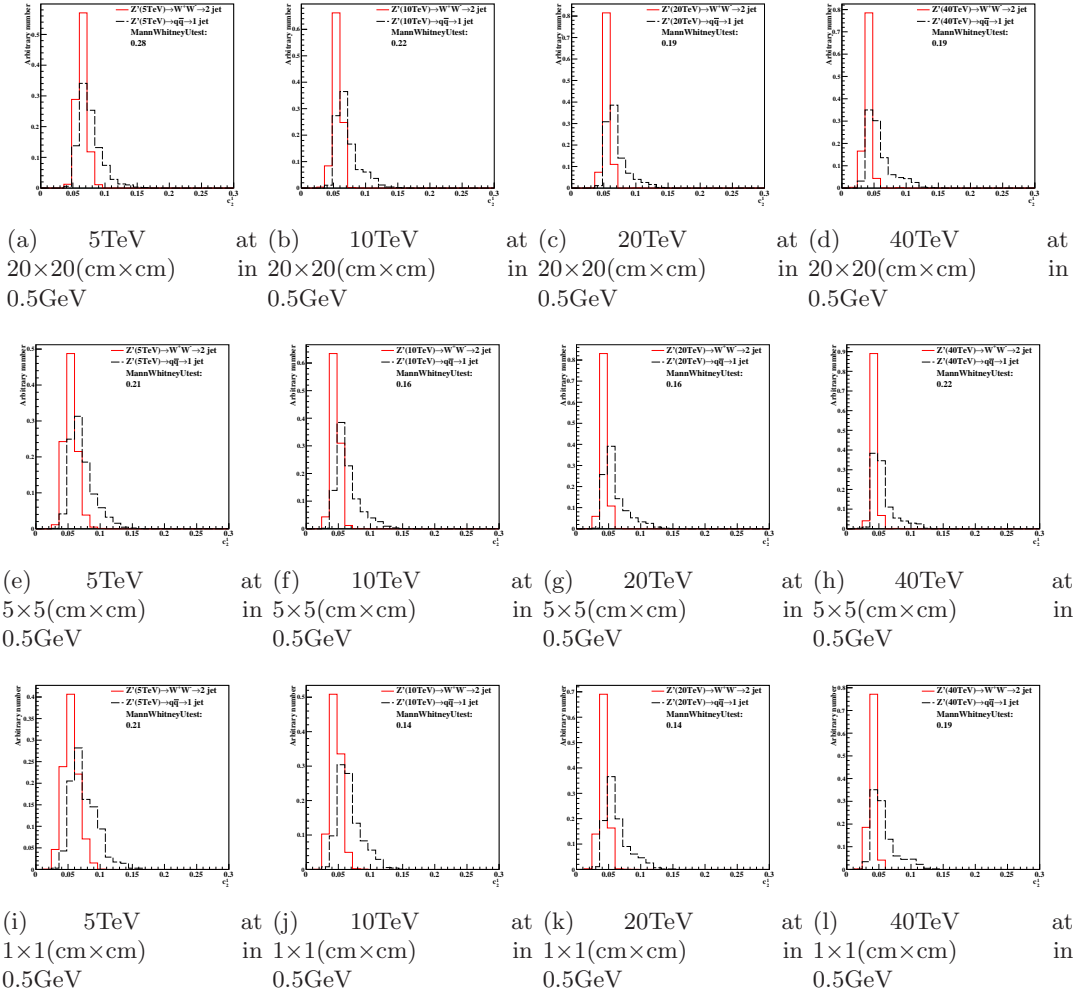
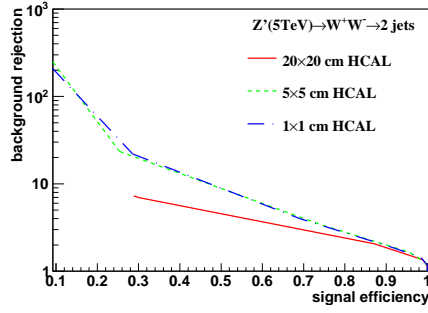
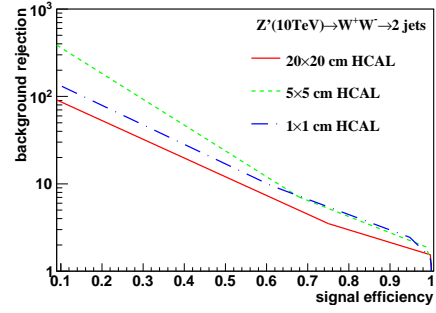


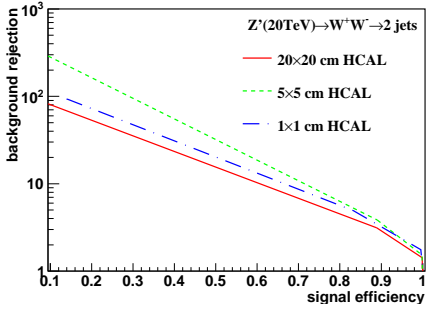
Figure 11: Distributions of Mann-Whitney value U in 5, 10, 20, 40TeV energy collision for c2b1 in different detector sizes. Cell Size in  $20 \times 20$ ,  $5 \times 5$ , and  $1 \times 1 (\text{cm} \times \text{cm})$  are shown here.



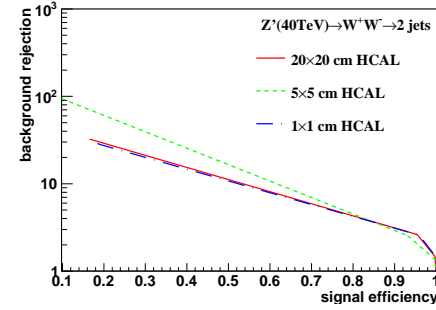
(a) 5 TeV using Rawhit 0.5GeV cut method with New2 after cut Method



(b) 10 TeV using Rawhit 0.5GeV cut method with New2 after cut Method



(c) 20 TeV using Rawhit 0.5GeV cut method with New2 after cut Method



(d) 40 TeV using Rawhit 0.5GeV cut method with New2 after cut Method

Figure 12: Signal efficiency versus background rejection rate using c2b1. The energies of collision at (a)5, (b)10, (c)20, (d)40TeV are shown here. In each picture, the three ROC curves correspond to different detector sizes.

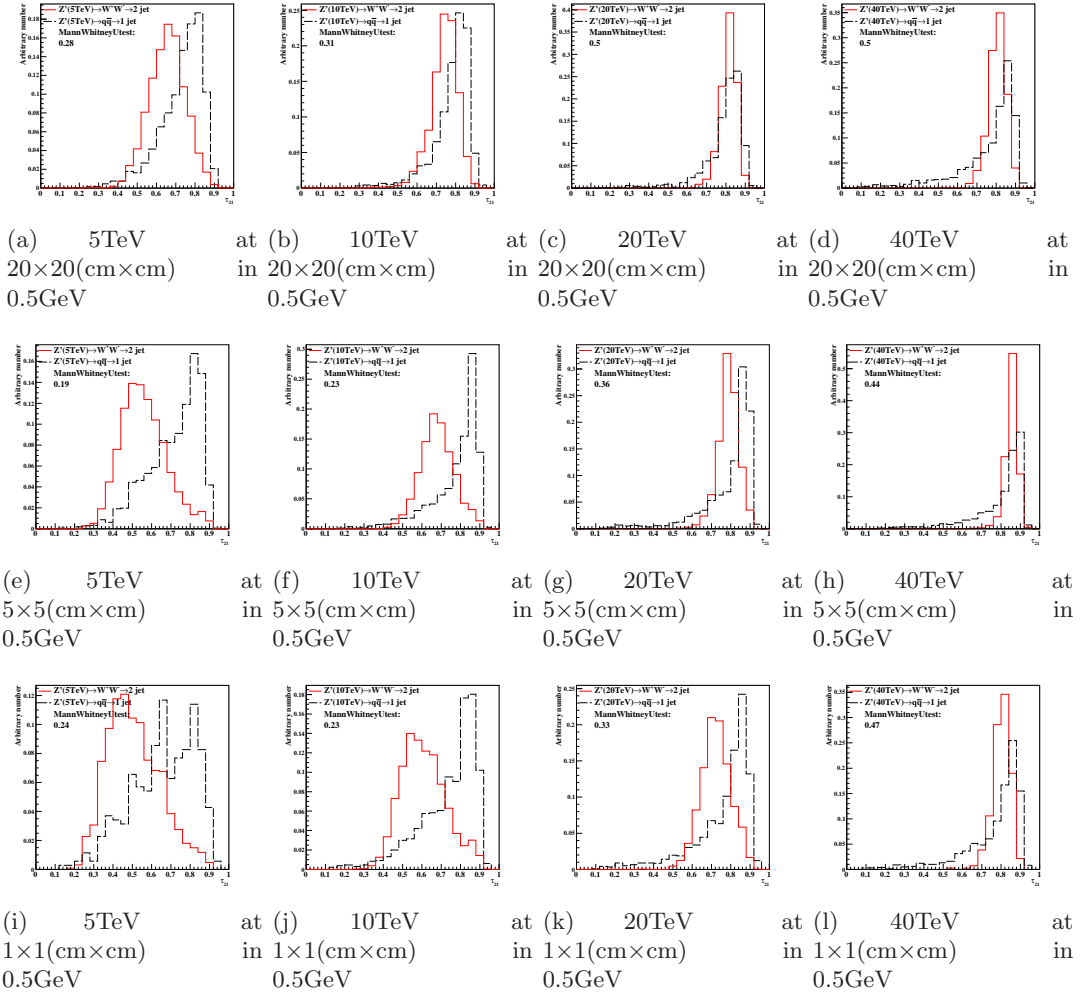
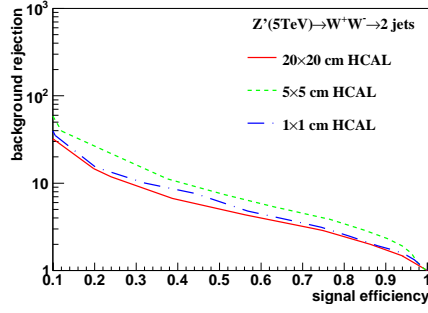
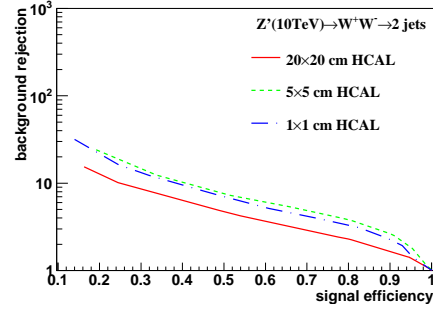


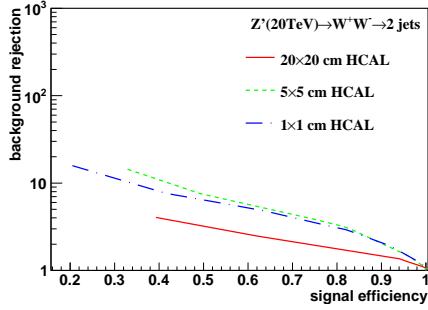
Figure 13: Distributions of Mann-Whitney value  $U$  in 5, 10, 20, 40TeV energy collision for  $\tau_{21}$  in different detector sizes. Cell Size in  $20 \times 20$ ,  $5 \times 5$ , and  $1 \times 1 (\text{cm} \times \text{cm})$  are shown here.



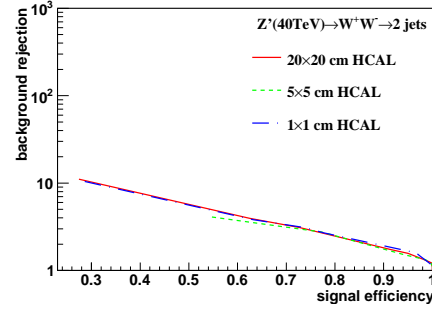
(a) 5 TeV using Rawhit 0.5GeV cut method with New2 after cut Method



(b) 10 TeV using Rawhit 0.5GeV cut method with New2 after cut Method



(c) 20 TeV using Rawhit 0.5GeV cut method with New2 after cut Method



(d) 40 TeV using Rawhit 0.5GeV cut method with New2 after cut Method

Figure 14: Signal efficiency versus background rejection rate using  $\tau_{21}$ . The energies of collision at (a)5, (b)10, (c)20, (d)40TeV are shown here. In each picture, the three ROC curves correspond to different detector sizes.

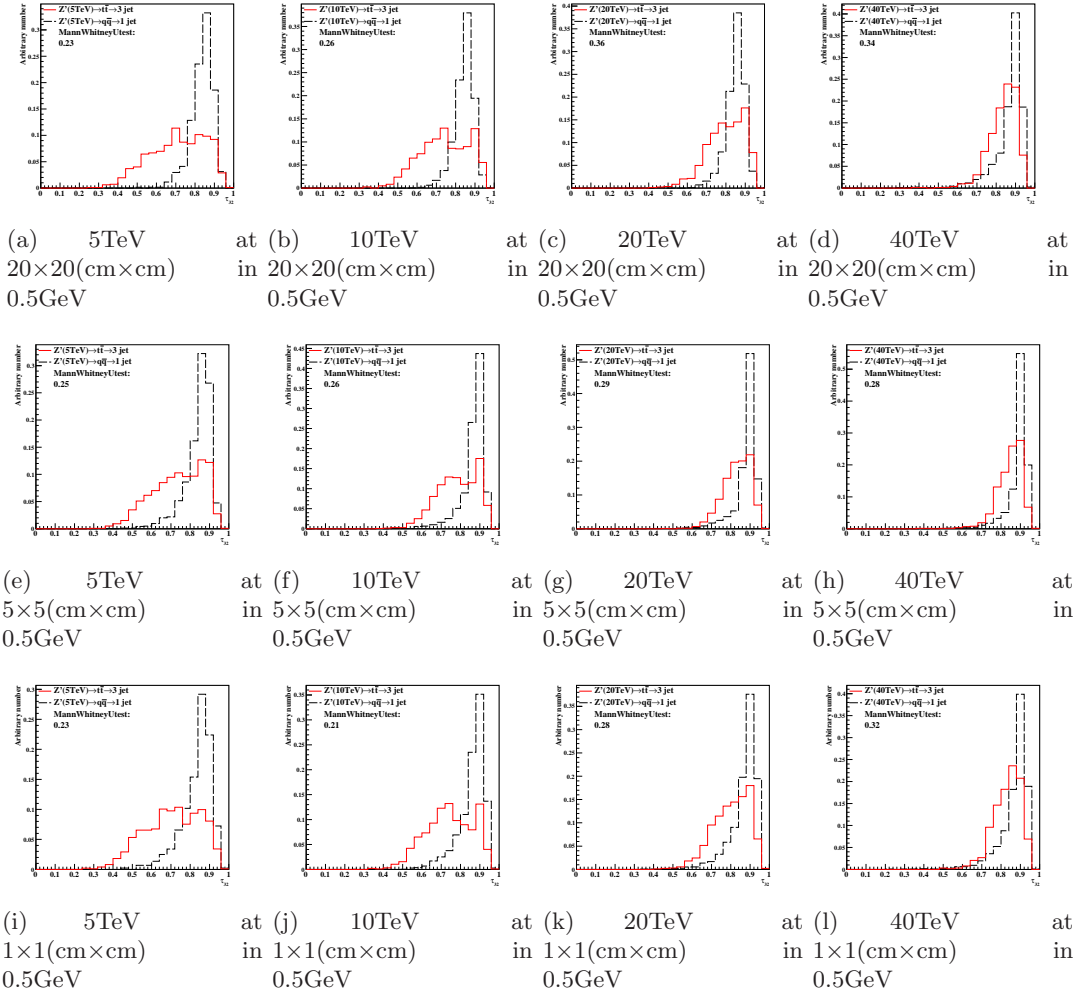
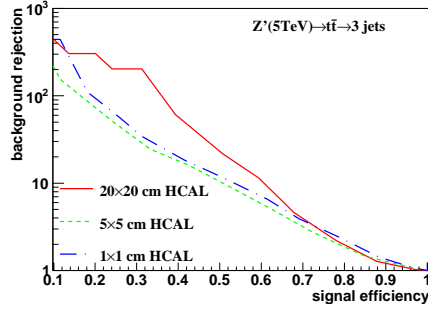
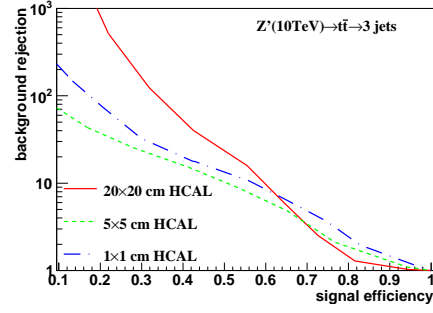


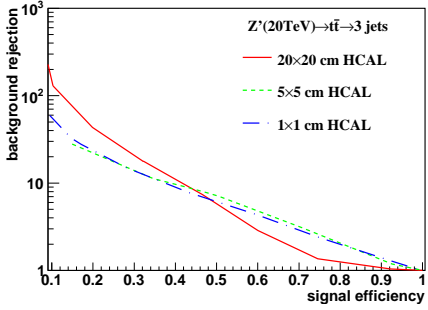
Figure 15: Distributions of Mann-Whitney value  $U$  in 5, 10, 20, 40TeV energy collision for  $\tau_{32}$  in different detector sizes. Cell Size in  $20 \times 20$ ,  $5 \times 5$ , and  $1 \times 1 (\text{cm} \times \text{cm})$  are shown here.



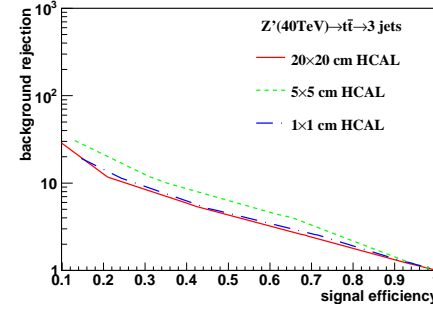
(a) 5 TeV using Rawhit 0.5GeV cut method with New2 after cut Method



(b) 10 TeV using Rawhit 0.5GeV cut method with New2 after cut Method

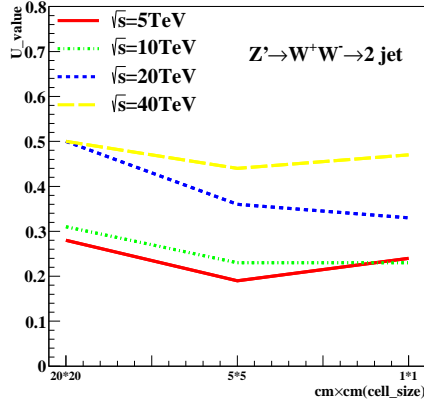


(c) 20 TeV using Rawhit 0.5GeV cut method with New2 after cut Method

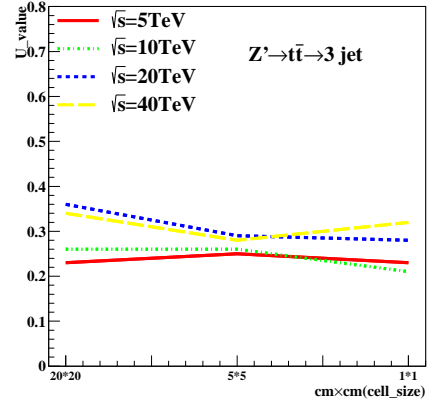


(d) 40 TeV using Rawhit 0.5GeV cut method with New2 after cut Method

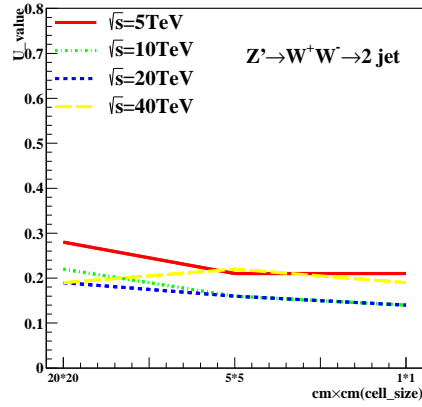
Figure 16: Signal efficiency versus background rejection rate using  $\tau_{32}$ . The energies of collision at (a)5, (b)10, (c)20, (d)40TeV are shown here. In each picture, the three ROC curves correspond to different detector sizes.



(a)  $\tau_{21}$  rawhit cut with 0.5GeV



(b)  $\tau_{32}$  rawhit cut with 0.5GeV



(c)  $c_2^{(1)}$  rawhit cut with 0.5GeV

Figure 17: The Mann-Whitney U values for  $\tau_{21}, \tau_{32}$  and  $c_2^{(1)}$  reconstructed from calorimeter hit at 0.5GeV cut with different collision energies correspond to different detector sizes in rawhit cut with 0.5GeV. The energies of collision at 5, 10, 20, 40, 20, 40TeV are shown in each figure.



## References

- [1] M. Benedikt, [The Global Future Circular Colliders Effort](#) CERN-ACC-SLIDES-2016-0016. Presented at P5 Workshop on the Future of High Energy Physics, BNL, USA, Dec. 15-18, 2013. URL <http://cds.cern.ch/record/2206376>
- [2] J. Tang, et al., Concept for a Future Super Proton-Proton Collider (2015). [arXiv:1507.03224](#).
- [3] R. Calkins, et al., [Reconstructing top quarks at the upgraded LHC and at future accelerators](#), in: Proceedings, Community Summer Study 2013: Snowmass on the Mississippi (CSS2013): Minneapolis, MN, USA, July 29-August 6, 2013. [arXiv:1307.6908](#). URL <https://inspirehep.net/record/1244676/files/arXiv:1307.6908.pdf>
- [4] S. V. Chekanov, J. Dull, Energy range of hadronic calorimeter towers and cells for high-pT jets at a 100 TeV collider [arXiv:1511.01468](#).
- [5] E. Coleman, M. Freytsis, A. Hinzmann, M. Narain, J. Thaler, N. Tran, C. Vernieri, The importance of calorimetry for highly-boosted jet substructure [arXiv:1709.08705](#).
- [6] DELPHES 3 Collaboration, J. de Favereau, C. Delaere, P. Demin, A. Giammanco, V. Lematre, A. Mertens, M. Selvaggi, DELPHES 3, A modular framework for fast simulation of a generic collider experiment, JHEP 02 (2014) 057. [arXiv:1307.6346](#), [doi:10.1007/JHEP02\(2014\)057](#).
- [7] S. V. Chekanov, M. Beydler, A. V. Kotwal, L. Gray, S. Sen, N. V. Tran, S. S. Yu, J. Zuzelski, Initial performance studies of a general-purpose detector for multi-TeV physics at a 100 TeV pp collider, JINST 12 (06) (2017) P06009. [arXiv:1612.07291](#), [doi:10.1088/1748-0221/12/06/P06009](#).
- [8] J. Allison, et al., Recent developments in Geant4, Nuclear Instruments and Methods in Physics Research A 835 (2016) 186.
- [9] M. J. Charles, PFA Performance for SiD, in: Linear colliders. Proceedings, International Linear Collider Workshop, LCWS08, and International Linear Collider Meeting, ILC08, Chicago, USA, November 16-20, 2008, 2009. [arXiv:0901.4670](#).
- [10] J. S. Marshall, M. A. Thomson, Pandora Particle Flow Algorithm, in: Proceedings, International Conference on Calorimetry for the High Energy Frontier (CHEF 2013), 2013, pp. 305–315. [arXiv:1308.4537](#).
- [11] G. P. S. M. Cacciari, G. Soyez, FastJet user manual CERN-PH-TH/2011-297. [arXiv:1111.6097](#).
- [12] M. Cacciari, G. P. Salam, G. Soyez, The anti-kt jet clustering algorithm, JHEP 0804 (2008) 063. [arXiv:0802.1189](#).
- [13] S. Chekanov, HepSim: a repository with predictions for high-energy physics experiments, Advances in High Energy Physics 2015 (2015) 136093, available as <http://atlaswww.hep.anl.gov/hepsim/>.
- [14] B. Auerbach, S. Chekanov, J. Love, J. Proudfoot, A. Kotwal, Sensitivity to new high-mass states decaying to ttbar at a 100 TeV collider [arXiv:1412.5951](#).
- [15] J. Butterworth, B. Cox, J. R. Forshaw, WW scattering at the CERN LHC, Phys.Rev. D65 (2002) 096014. [arXiv:hep-ph/0201098](#), [doi:10.1103/PhysRevD.65.096014](#).
- [16] S. Catani, Y. L. Dokshitzer, M. H. Seymour, B. R. Webber, [Longitudinally-invariant k-clustering algorithms for hadron-hadron collisions](#), Nuclear Physics B 406 (12) (1993) 187 – 224. URL <http://www.sciencedirect.com/science/article/pii/055032139390166M>
- [17] S. D. Ellis, D. E. Soper, Successive combination jet algorithm for hadron collisions, Phys. Rev. D48 (1993) 3160–3166. [arXiv:hep-ph/9305266](#), [doi:10.1103/PhysRevD.48.3160](#).
- [18] ATLAS Collaboration Collaboration, G. Aad, et al., Jet mass and substructure of inclusive jets in  $\sqrt{s} = 7$  TeV pp collisions with the ATLAS experiment, JHEP 1205 (2012) 128. [arXiv:1203.4606](#), [doi:10.1007/JHEP05\(2012\)128](#).
- [19] J. Thaler, K. Van Tilburg, Identifying Boosted Objects with N-subjettiness, JHEP 03 (2011) 015. [arXiv:1011.2268](#), [doi:10.1007/JHEP03\(2011\)015](#).
- [20] A. J. Larkoski, S. Marzani, G. Soyez and J. Thaler, JHEP **1405**, 146 (2014).
- [21] Y. L. Dokshitzer, G. D. Leder, S. Moretti and B. R. Webber, JHEP **9708**, 001 (1997).
- [22] M. Wobisch and T. Wengler, In \*Hamburg 1998/1999, Monte Carlo generators for HERA physics\* 270-279.